

# Stress-Actuated Spiral Microelectrode for High-Performance Lithium-Ion Microbatteries

Hongmei Tang, Dmitriy D. Karnaushenko, Volker Neu, Felix Gabler, Sitao Wang, Lixiang Liu, Yang Li, Jiawei Wang, Minshen Zhu,\* and Oliver G. Schmidt

Miniaturization of batteries lags behind the success of modern electronic devices. Neither the device volume nor the energy density of microbatteries meets the requirement of microscale electronic devices. The main limitation for pushing the energy density of microbatteries arises from the low mass loading of active materials. However, merely pushing the mass loading through increased electrode thickness is accompanied by the long charge transfer pathway and inferior mechanical properties for long-term operation. Here, a new spiral microelectrode upon stress-actuation accomplishes high mass loading but short charge transfer pathways. At a small footprint area of around 1 mm<sup>2</sup>, a 21-fold increase of the mass loading is achieved while featuring fast charge transfer at the nanoscale. The spiral microelectrode delivers a maximum area capacity of 1053 μAh cm<sup>-2</sup> with a retention of 67% over 50 cycles. Moreover, the energy density of the cylinder microbattery using the spiral microelectrode as the anode reaches 12.6 mWh cm<sup>-3</sup> at an ultrasmall volume of 3 mm<sup>3</sup>. In terms of the device volume and energy density, the cylinder microbattery outperforms most of the current microbattery technologies, and hence provides a new strategy to develop high-performance microbatteries that can be integrated with miniaturized electronic devices.

cell with a volume of 2.3 cm<sup>3</sup> delivers an energy density of 800 mWh cm<sup>-3</sup> while it drops to 463 mWh cm<sup>-3</sup> as the volume decreases to 1.1 cm<sup>3</sup>.<sup>[9]</sup> Apparently, very limited energy is stored in a microbattery if the energy density and volume of the device decrease simultaneously. On the one hand, the packaging consumes a large portion of the volume. On the other hand, limited energy is attributed to the decreasing mass loading when the battery volume scales down. Both of these two factors impose the importance of high mass loading at a minimal volume of the battery. If we take the size of surface mount devices as the reference size for microbatteries, their volume should be restricted to ≈100 mm<sup>3</sup>. However, at these volumes, the energy density delivered by most microbattery technologies is even less than 10 mWh cm<sup>-3</sup>, which significantly limits the application scenarios of microbatteries.<sup>[10]</sup> Therefore, the development of high-energy-density microbat-

teries with a volume less than 100 mm<sup>3</sup> remains a significant challenge to overcome.

The low energy density of existing microbatteries is attributed to the limited active material loading. Given that microbatteries occupy tiny areas, high mass loading on a minimal footprint area is a crucial metric in microbattery development.<sup>[11]</sup> The current roadmap to tackle the challenge of high mass loading includes two strategies: first, producing interdigitated configurations over thick films, and second generating fully

teries with a volume less than 100 mm<sup>3</sup> remains a significant challenge to overcome.

The low energy density of existing microbatteries is attributed to the limited active material loading. Given that microbatteries occupy tiny areas, high mass loading on a minimal footprint area is a crucial metric in microbattery development.<sup>[11]</sup> The current roadmap to tackle the challenge of high mass loading includes two strategies: first, producing interdigitated configurations over thick films, and second generating fully

H. Tang, Dr. D. D. Karnaushenko, Dr. V. Neu, F. Fabler, S. Wang, L. Liu, Dr. J. Wang, Dr. M. Zhu, Prof. O. G. Schmidt  
Institute for Integrative Nanosciences  
Dresden 01069, Germany  
E-mail: m.zhu@ifw-dresden.de

 The ORCID identification number(s) for the author(s) of this article can be found under <https://doi.org/10.1002/sml.202002410>.

© 2020 The Authors. Published by WILEY-VCH Verlag GmbH & Co. KGaA, Weinheim. This is an open access article under the terms of the Creative Commons Attribution-NonCommercial-NoDerivs License, which permits use and distribution in any medium, provided the original work is properly cited, the use is non-commercial and no modifications or adaptations are made.

DOI: 10.1002/sml.202002410

H. Tang, F. Gabler, L. Xiang, Y. Li, Prof. O. G. Schmidt  
Material Systems for Nanoelectronics  
Technische Universität Chemnitz  
Chemnitz 09107, Germany

H. Tang, F. Gabler, L. Liu, Y. Li, Prof. O. G. Schmidt  
Center for Materials, Architectures, and Integration of Nanomembranes (MAIN)  
Technische Universität Chemnitz  
Chemnitz 09126, Germany  
Prof. O. G. Schmidt  
Nanophysics  
Faculty of Physics  
Technische Universität Dresden  
Dresden 01062, Germany

interdigitated configurations based on porous and interconnected scaffolds.<sup>[2,10,12]</sup> The former strategy improves the energy storage performance by simply transforming the configuration from thin films to thick films. However, the increased diffusion paths and weakened mechanical integrity of the thick electrode are severe bottlenecks for the energy storage performance of the interdigitated thick-film design.<sup>[13]</sup> Moreover, gaps between interdigitated electrodes waste the valuable volume of microbatteries. As a result, the interdigitated thick-electrode configurations hardly exceed the performance of conventional thin-film batteries. Fully interdigitated configurations are regarded as 3D design, which effectively improve the space utilization of microbatteries and mass loading of active materials.<sup>[2,12,14–18]</sup> As a result, fully interdigitated configured microbatteries deliver record high areal capacities of up to 1.8 mAh cm<sup>-2</sup>. However, the porous and interconnected scaffolds occupy large footprint areas of about 9 mm<sup>2</sup>, which are much larger than for currently available microscale energy supplies, such as surface mount capacitors (≈1 mm<sup>2</sup>) used in electronic devices.<sup>[2]</sup> In short, both of the current strategies are successful in increasing the mass loading of active materials but fails in the simultaneous reduction of the footprint area, which is critical in microelectronics. Therefore, a new challenge, the realization of high mass loading of electrode materials and the reduction of the footprint area, has emerged and is remaining unsolved.

Apart from novel architectures for microbatteries, the use of high capacity electrode materials that can deliver a high capacity at a minimal mass loading can further improve the energy storage performance of microbatteries.<sup>[19,20]</sup> Regarding high capacity electrode materials, silicon has a capacity density of 3579 mAh g<sup>-1</sup>, which is beneficial to enhance the energy density of microbatteries with limited mass loading.<sup>[21,22]</sup> However, silicon anodes suffer from fast capacity degradation and poor rate capability because silicon shows low conductivity and lithium ion diffusivity, as well as sizeable volumetric variations during the charge/discharge process.<sup>[23,24]</sup> To improve the performance of silicon anodes, nanoengineering the silicon anode with other durable and conductive nanomaterials, such as graphene, has been effective.<sup>[25–27]</sup> However, the chemical synthesis routes are not compatible with most microfabrication technologies. Alternatively, combining silicon with germanium harnesses the high conductivity and lithium ion diffusivity of germanium and the high capacity of silicon.<sup>[28,29]</sup> Meanwhile, nanostructuring silicon–germanium (Si–Ge) compounds can effectively prevent the electrode pulverization, which improves the cycling stability of the anode.<sup>[30]</sup> However, nanoengineering microscale devices usually contradicts the goal to achieve a high mass loading of active materials within a minimal footprint area. Therefore, a new technology requires the versatility in integrating two incompatible strategies into the development of a high energy-density microbattery.

Here, we develop a prototype of a spiral microelectrode based on the Si–Ge compound. The spiral configuration is achieved by a self-assembly process driven by the internal stress in the layered nanomembrane.<sup>[31,32]</sup> This new technology simultaneously reduces the footprint area and increases the mass loading to 21 times per unit area compared to its 2D counterpart. Moreover, the unique spiral structure simultaneously maintains the short charge transfer pathway of the nanomembrane, which circumvents the problem of a long path for the charge transfer

in a thick and high-mass-loading electrode. The Si–Ge spiral microelectrode is used as a robust and freestanding micro-anode in the lithium-ion microbattery, which delivers a maximum areal capacity of 1053 μAh cm<sup>-2</sup> and shows a stable cycling performance (67%). Moreover, the high-energy storage performance of the Si–Ge spiral microelectrode enables the fabrication of a high-energy microbattery with an ultrasmall package volume of 3 mm<sup>3</sup>. The energy density achieved in such a small size reaches 12.6 mWh cm<sup>-3</sup>, which even surpasses the performance of most commercial microbatteries with much larger volumes. Therefore, the unique spiral microelectrodes (sp-μEDs) pave a new way for the development of high-performance microbatteries.

Increasing the thickness of the active electrode materials intuitively boosts the mass loading and hence enhances the energy storage ability. However, a considerable thickness produces a long pathway for charge transport, which impairs the energy storage performance of the electrode (**Figure 1a**).<sup>[33]</sup> **Figure 1b** shows the experimental relationship between thickness and the areal capacity of the Si–Ge layered electrodes in a coin cell. The blue dots are the experimental value while the red dot line shows the expected trend. The starting thickness of Si and Ge for the compound electrode is 60 and 20 nm, respectively (corresponding to the thickness increase factor of 1). It is evident that the capacity increases nonlinearly with increasing thickness of the Si–Ge bilayer nanomembrane. Moreover, rather than increasing continuously, the capacity drops when the thickness of Si–Ge increases by a factor of ten. This unexpected phenomenon clearly shows the disadvantage of merely pushing the thickness of the compound electrode. The slow ion transportation through thick films limits the capacity. In addition, the instability of the Si–Ge electrode is exacerbated for a thick electrode because of the substantial volume change of the Si and Ge during the charge/discharge cycles.<sup>[34]</sup> As shown in **Figure 1c**, the thinnest Si–Ge electrode shows a stable cycling performance. With increasing thickness, the capacity fades quickly over cycling. When the factor reaches 6, the capacity starts to fluctuate due to the poor integrity of the electrode. With a thickness increase factor of 10, the capacity drastically drops after 5 cycles, which is attributed to the destruction of the electrode.<sup>[35]</sup> Intriguingly, after 30 cycles, the thinnest electrode delivers the lowest capacity drop, which is attributed to the smaller stress in the layer due to anisotropic expansion of the material, thus improving the cycling stability.<sup>[36]</sup> Keeping in mind that the microelectrode possesses a tiny footprint area, which will aggravate the structural failure of a thick electrode, it is clear that the enhancement of the energy density of a microelectrode requires a solution that combines the best of both worlds: retaining the robust structure of the ultrathin nanomembrane but loading a large quantity of active materials at a minimal footprint area.

In addition, cracking and corrugation of deposited nanomembranes are typical phenomena due to the internal stress. Extensive efforts have been devoted to minimizing this stress-driven effect because deposited nanomembranes are expected to adhere well without cracks. Conversely, the stress-actuation may translate this negative effect into an efficient way to reshape the nanomembranes into a 3D micro-object.<sup>[37–43]</sup> In principle, internal stress arises during the vacuum-deposited nanomembranes.<sup>[44,45]</sup> **Figure S1**, Supporting Information, shows that the sequential vacuum deposition produces tensile

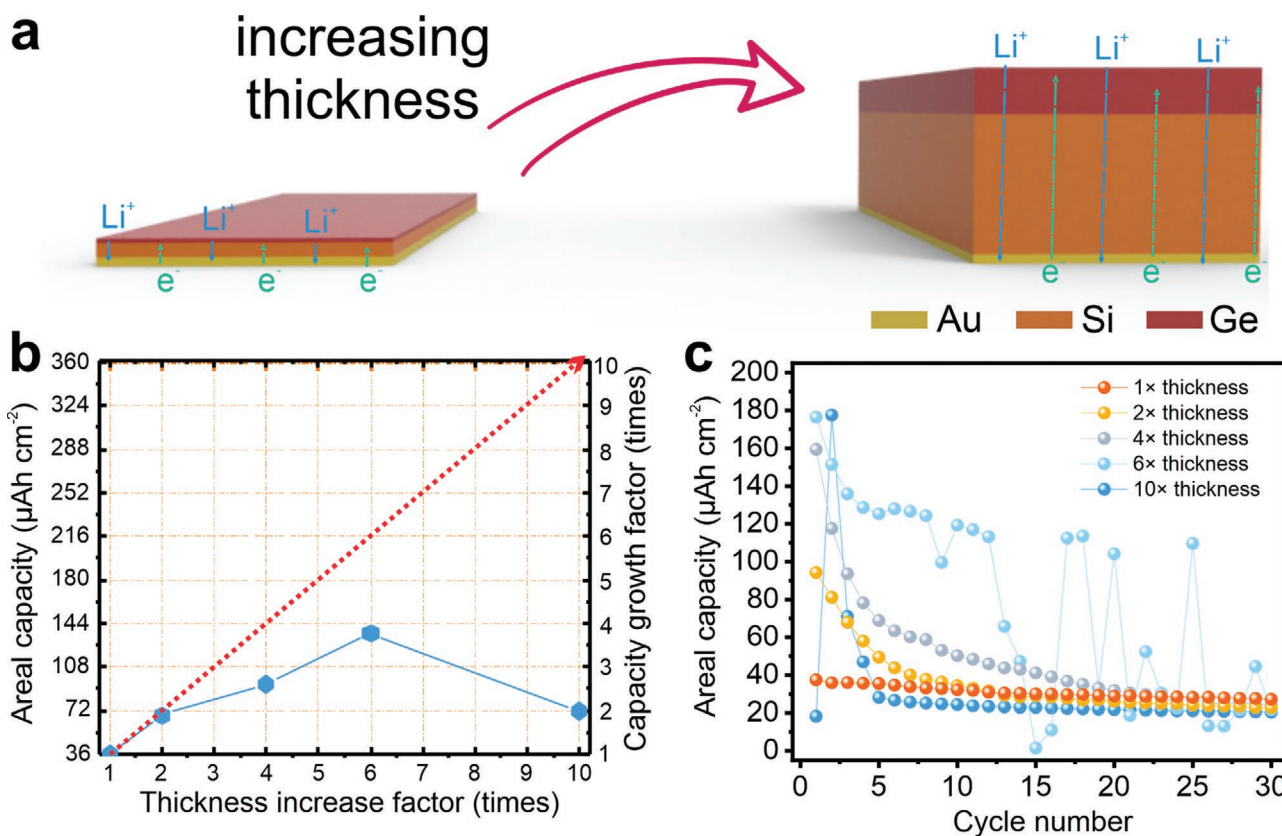


**Figure 1.** a) Schematic illustration of ion diffusion and charge transport path in the electrode. Evolution of b) areal capacity and c) cycling performance of the Si–Ge compound with different thickness increase factors.

stress of 120 MPa at the top layer (interface of the Si–Ge bilayer structure) while a 330 MPa compressive stress arises at the bottom layer (Au–Si interface). The established force field will subsequently drive the layered nanomembrane into a spiral structure. A finite element method (FEM) is used to simulate the self-assembly process of the Si–Ge compound nanomembrane with the thickness increase factor of 1. As shown in **Figure 2a**, the internal stress triggers the roll-up process of the compound nanomembrane and forms a “swiss-roll,” which features a “quasi-stacked” structure (magnified image of the “swiss-roll”). Moreover, the interlayer gap in the “quasi-stacked” structure and nanometer thickness of each winding enable a fast charge transfer, which perfectly resolves the disadvantage of sluggish charge transport in thick microelectrodes (**Figure 2b**).<sup>[46]</sup> Experimentally, we designed a self-assembly technology to create freestanding sp- $\mu$ EDs. This simple technology requires one lithography process, which simultaneously defines the size of the Si–Ge nanomembrane and the preferential rolling direction (**Figure S2**, Supporting Information). Au, Si, and Ge were deposited sequentially onto the patterned sacrificial layer (photoresist) by physical vapor deposition. The X-ray diffraction (XRD) patterns show broad and weak peaks of both Si and Ge, indicating the nanocrystalline or even amorphous structure (**Figure S3a**, Supporting Information). Afterward, the release process of the intrinsic stress was controlled by the progressive etching of the photoresist sacrificial layer beneath the Si–Ge compound nanomembrane. As a result,

we successfully fabricated Si–Ge sp- $\mu$ EDs without cracks (**Figure S4**, Supporting Information). After the roll-up process, the gold layer, serving as the conductive additive layer, is exposed at the outermost layer. Therefore, three diffraction peaks of the Si–Ge sp- $\mu$ EDs, in good agreement with those of Au (JCPDS file: 04–0784), are observed in the XRD patterns (**Figure S3a**, Supporting Information). The Si and Ge peaks are observed if we grind the Si–Ge sp- $\mu$ EDs into powders (**Figure S3b**, Supporting Information). As the spiral electrode is formed by a mechanical transformation from the thin-film system, the crystalline and crystallite size of materials should be identical with the thin-film system. The average external diameter of the Si–Ge sp- $\mu$ EDs is around 160  $\mu\text{m}$  (**Figure S5a**, Supporting Information). **Figure 2c** shows the scanning electron microscope (SEM) image of the cross section of the Si–Ge sp- $\mu$ ED, which resembles that of a spiral structure. The spiral structure effectively scales down the footprint area of the original nanomembrane electrode (from 24.7 to 1.1  $\text{mm}^2$ ; **Figure S5b**, Supporting Information). The scale-down ratio determines the thickness increase factor of the Si–Ge sp- $\mu$ ED. The large factor of 21 demonstrates the accomplishment of high mass loading of a microelectrode at minimal footprint area. **Figure 2d** shows the parallel production of Si–Ge sp- $\mu$ EDs, which proves the robustness of the stress-actuated self-assembly process. Moreover, thanks to the freestanding nature of the as-fabricated Si–Ge sp- $\mu$ EDs, we directly use single Si–Ge sp- $\mu$ EDs as the working electrodes to test the energy storage performance. To

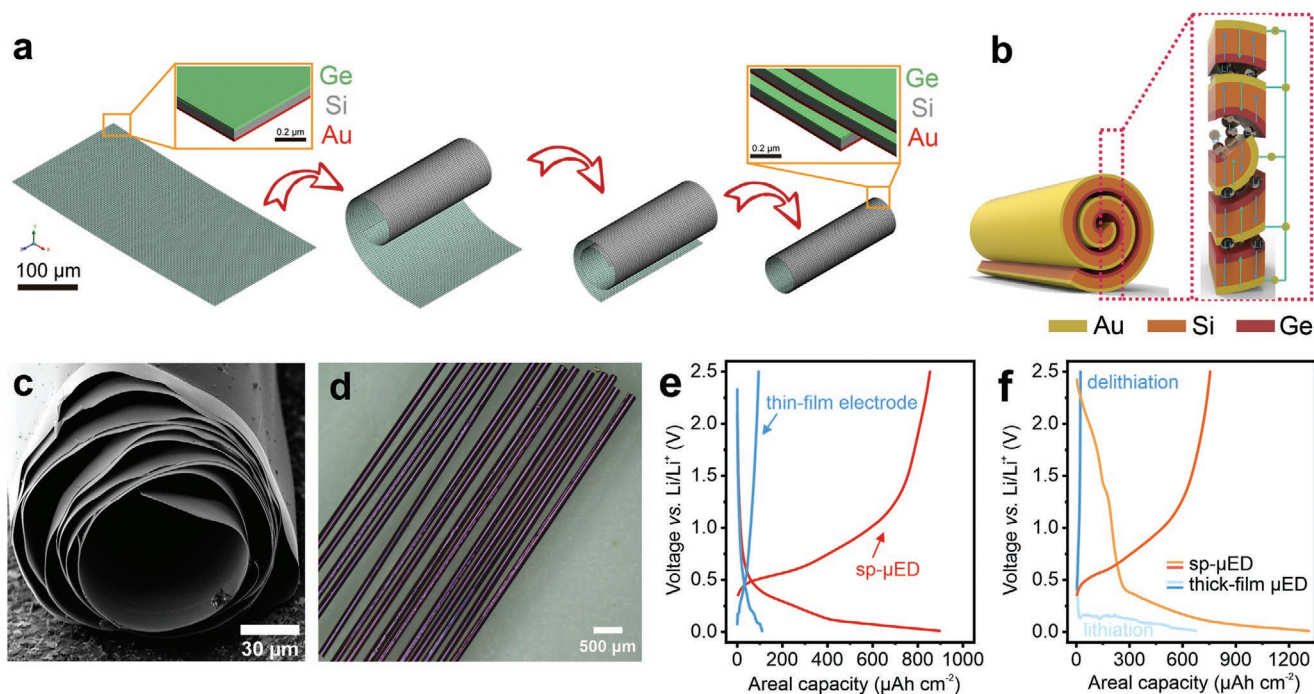


**Figure 2.** a) Finite element simulation of Si–Ge compound with conductive support (Au: 5 nm, Si: 60 nm, Ge: 20 nm). b) Schematic illustration of ion diffusion and charge transport path of the spiral electrode. c) SEM image of the cross section of the Si–Ge sp- $\mu$ ED. d) Optical microscope image of Si–Ge sp- $\mu$ EDs. e) Comparison of the charge/discharge profile of Si–Ge sp- $\mu$ EDs and the thin-film electrode within 0.01–2.5 V versus Li/Li<sup>+</sup> at 9.42  $\mu$ A. f) Comparison of the charge/discharge profile of the Si–Ge sp- $\mu$ ED and thick-film microelectrode within 0.01–2.5 V versus Li/Li<sup>+</sup> at 9.42  $\mu$ A (0.83 mA cm<sup>-2</sup>).

establish the electric connection between the freestanding electrode and the current collector, we use silver paste to bind the electrode and current collector. The capacity contribution from the silver paste is recorded in Figure S6, Supporting Information. The capacity contribution from the silver paste is less than 2%. Therefore, the silver paste provides a stable electric connection but contributes little to the capacity. Figure 2e compares the areal capacity of the 2D Si–Ge compound nanomembrane electrode and the Si–Ge sp- $\mu$ ED. The capacity of Si–Ge sp- $\mu$ ED increases by nine times compared to the nanomembrane electrode. The dramatic increase in areal capacity proves the effectiveness of the enhancement of energy density by the spiral structure. Furthermore, Figure 2e compares the areal capacity of the thick microelectrode and the sp- $\mu$ ED with the same footprint area and mass loading. The magnified voltage profiles are shown in Figure S7, Supporting Information. An intensive lithiation process is observed below 0.5 V for both microelectrodes, indicating similar electrochemical behavior. The subtle difference in the lithiation plateaus is attributed to the different layer stacks and bulk resistance. For the sp- $\mu$ ED, the Ge layer is in the inner side while it is the outer layer for the thick microelectrode. Meanwhile, owing to the freestanding feature, the bulk resistance of the sp- $\mu$ ED may be larger than that of the thick microelectrode. As a result, the lithiation plateaus of the sp- $\mu$ ED are not as obvious as those of the thick microelectrode. It is evident that the lithiation capacity of the thick microelectrode is smaller than the sp- $\mu$ ED, which is attributed to the long charge transfer pathways. Moreover, the thick microelectrode cannot accommodate the substantial volume change of the Si and Ge during the lithiation process. As a result, the

de-lithiation capacity decreases significantly.<sup>[47]</sup> On the contrary, the sp- $\mu$ ED delivers a reversible capacity of 755  $\mu$ Ah cm<sup>-2</sup> after the first lithiation process, which indicates the spiral structure is robust enough to sustain the significant volume change. The gravimetric capacity calculated from the theory weight of the deposited Si and Ge layers reaches 2000 mAh g<sup>-1</sup>, indicating a high utilization of active materials. This feature further demonstrates the effectiveness of the spiral structure in improving the areal capacity without the sacrifice in the utilization of active materials.

Although Si–Ge sp- $\mu$ EDs can accommodate the volume change to some extent, the repetitive volume change during the cycling test leads to the fatigue of the structure and finally destroys the microelectrode. As shown in Figure 3a, the capacity of the Si–Ge sp- $\mu$ ED continuously decays over cycling. At the 37th cycle, the capacity drops dramatically, indicating the breakdown of the Si–Ge sp- $\mu$ ED. On the other hand, such sudden change is not observed in the thin-film electrode. Figure 3b shows the SEM image of the post-cycled Si–Ge sp- $\mu$ ED. Before cycling, the intact structure of the Si–Ge sp- $\mu$ ED is observed (inset in Figure 3b). By contrast, the Si–Ge sp- $\mu$ ED cracks into pieces after the cycling test. Owing to the freestanding nature, the fractured Si–Ge sp- $\mu$ ED will lose contact with the current collector, thus resulting in the failure of the battery. The Raman spectrum of the Si–Ge sp- $\mu$ ED after cycling also shows the emergence of Ge peaks due to the breakdown of the microelectrode (Figure S8, Supporting Information), which further confirms the structural instability at the extended charge/discharge cycles.<sup>[48]</sup> The occurrence of Ge peaks also indicates that the Si and Ge would not form the alloy over cycling. Therefore, it is

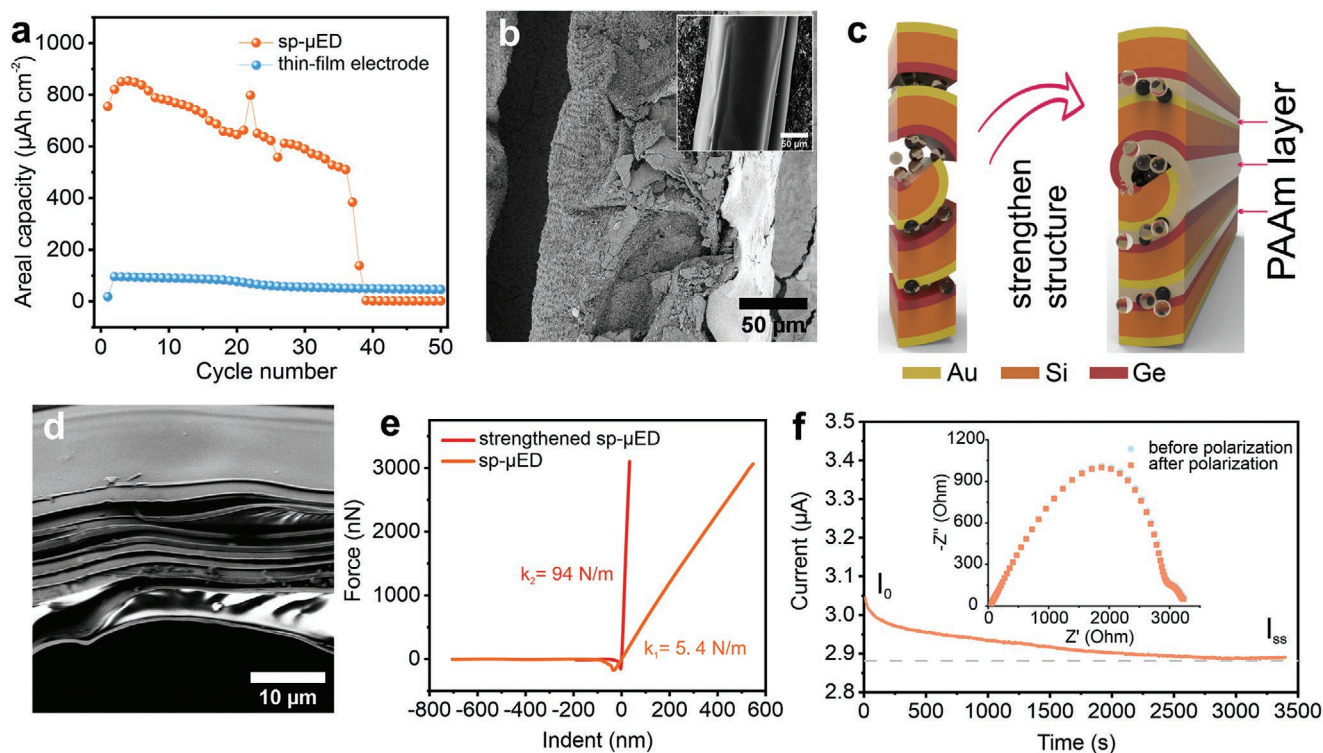


**Figure 3.** a) Cycling stability of Si-Ge sp-μED and Si-Ge thin-film electrode at 9.42 μA from 0.01 to 2.5 V. b) SEM image of Si-Ge sp-μED after cycling test. The inset shows the corresponding SEM image of the fresh electrode. c) Schematic illustration and d) SEM image of the strengthened Si-Ge sp-μED. e) Stiffness of Si-Ge sp-μEDs before and after strengthening. f) Variation of current with time during polarization of lithium symmetric cell containing PAAM at an applied voltage of 10 mV; the inset figure shows the Nyquist plots before and after polarization.

of great importance to strengthen the structural integrity of the Si-Ge sp-μED with the nanoscale geometry.

Figure 3c illustrates the strategy of integrating a strengthening layer with good mechanical properties. Here, we chose polyacrylamide (PAAm), a highly elastic polymer, as the mechanical strengthener. The PAAm is robust to sustain the mechanical deformation due to the compression and releasing of the hydrogen bonding.<sup>[49]</sup> Figure 3d shows the cross section of the Si-Ge sp-μED after the addition of the PAAm, in which windings are affixed by the PAAm. Figure 3e shows the mechanical properties of the Si-Ge sp-μEDs. After being strengthened by PAAm, the stiffness of the Si-Ge sp-μED increases from 5.4 to 94 N m<sup>-1</sup>. The significant improvement of the stiffness is attributed to the compact structure with a strengthening layer, which can reinforce the structural integrity under mechanical deformations. In addition to the enhancement of the mechanical property, PAAm should allow the transport of lithium ions. The transference number of lithium ions in the PAAm was measured by using a symmetric Li/Li cell and calculated by the Equation (1).<sup>[50,51]</sup>

$$t_+ = \frac{I_{ss}(\Delta V - I_0 R_0)}{I_0(\Delta V - I_{ss} R_{ss})} \quad (1)$$

where  $\Delta V$  is the applied potential (10 mV),  $R_0$  and  $R_{ss}$  are the electrode resistances before and after polarization, respectively.  $I_0$  and  $I_{ss}$  are the initial current and steady-state current, respectively. Figure 3f shows the current change under the 10 mV bias.

The inset displays the Nyquist plots of the fresh and the polarized symmetric cell. The values of  $R_0$  and  $R_{ss}$  were determined by fitting the Nyquist plots as listed in Table S1, Supporting Information. Accordingly, the lithium transference number of PAAm is 0.61, which is similar to the value of 0.66 of the standard electrolyte (Figure S9 and Table S1, Supporting Information). Apparently, PAAm shows high permeability for the lithium ions, which maintains the excellent energy storage performance.<sup>[52]</sup> Furthermore, the ionic conductivity after the addition of PAAm is good enough to maintain the electrochemical performance (Figure S10, Supporting Information).

Figure 4a shows the CV curves of the strengthened Si-Ge sp-μED in the range of 0.01 to 2.5 V versus Li/Li<sup>+</sup> at a scanning rate of 0.1 mV s<sup>-1</sup>. In the first cycle, a sharp cathodic peak at around 0.02 V and a weak reductive peak at 0.25 V correspond to the lithium insertion into Si and Ge, which forms amorphous Li<sub>x</sub>Si and Li<sub>x</sub>Ge.<sup>[29,53]</sup> The anodic peak centered at 0.51 V is ascribed to the co-delithiation of a-Li<sub>x</sub>Si and a-Li<sub>x</sub>Ge.<sup>[23]</sup> Similar electrochemical behaviors can be observed at a higher scan rate (Figure S11, Supporting Information), indicating a good rate performance. It is noteworthy that no distinctive solid electrolyte interface (SEI) formation peak is observed. On the contrary, this peak is observed at 0.48 V for the Si-Ge sp-μED without PAAm (Figure S11a, Supporting Information), indicating that the addition of PAAm can effectively suppress the formation of a dense SEI layer by limiting the decomposition of the electrolyte on the electrode surface. The galvanostatic charge/discharge profiles are shown in Figure 4b. Consistent

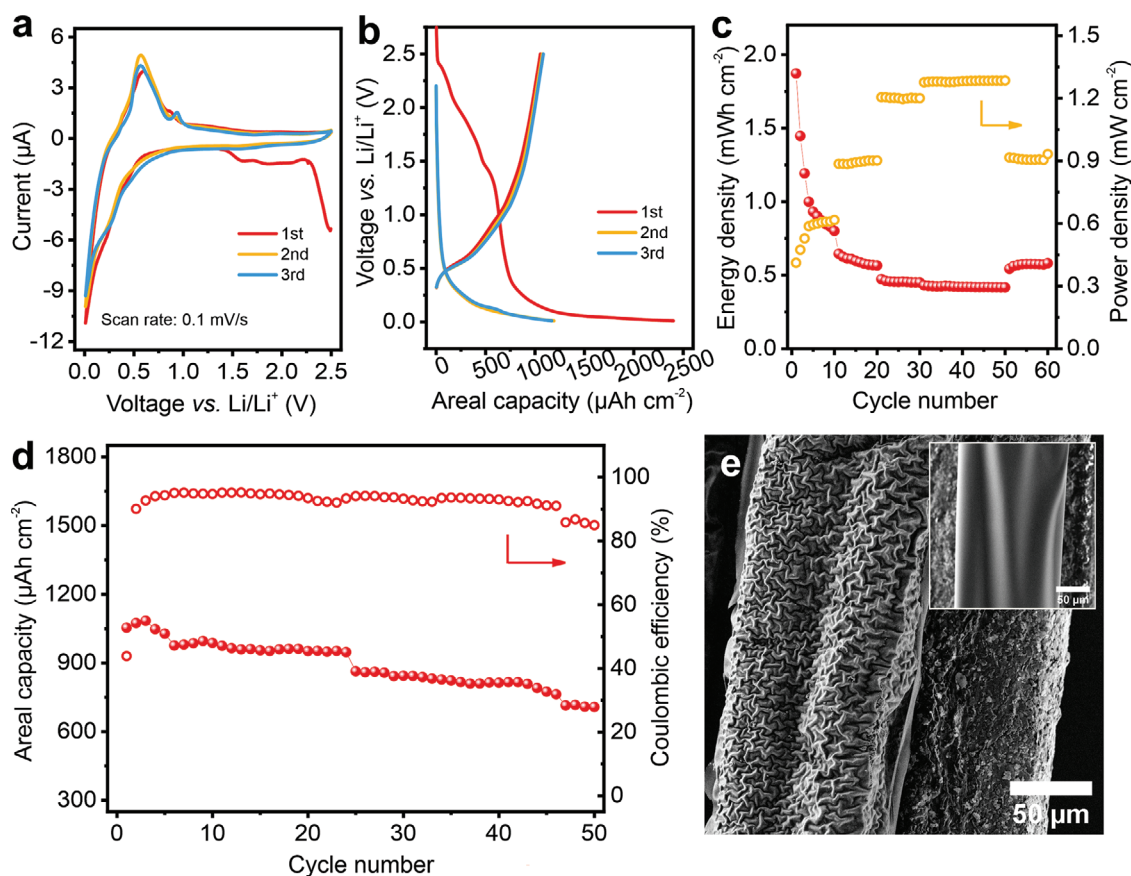


**Figure 4.** a) CV curves at  $0.1 \text{ mV s}^{-1}$  and b) charge/discharge profiles of strengthened Si-Ge sp- $\mu$ EDs over the first three cycles at  $9.42 \text{ } \mu\text{A}$  ( $0.83 \text{ mA cm}^{-2}$ ). c) Rate capability at different current densities from  $0.65$  to  $1.04 \text{ mA cm}^{-2}$  and d) cycling stability of the strengthened Si-Ge sp- $\mu$ ED from  $0.01$  to  $2.5 \text{ V}$  at  $0.83 \text{ mA cm}^{-2}$ . e) SEM image of strengthened Si-Ge sp- $\mu$ ED after cycling test; the inset shows the corresponding SEM image of the fresh electrode.

with the CV curves, no obvious SEI formation is observed at around  $0.5 \text{ V}$  for the strengthened Si-Ge sp- $\mu$ ED while a plateau corresponding to the SEI formation is observed for the sp- $\mu$ ED without PAAm (Figure S11b, Supporting Information). After the first cycle, a maximum capacity of  $1053 \text{ } \mu\text{Ah cm}^{-2}$  is achieved. The weight of PAAm is neglectable due to the ultralow concentration of the PAAm solution ( $0.5 \text{ wt}\%$ ). As a result, the addition of PAAm will not lower the energy density. Figure 4c shows the rate performance of the strengthened Si-Ge sp- $\mu$ ED. The energy density decreases with increasing power density. At a high power density of  $1.28 \text{ mW cm}^{-2}$ , the energy density still reaches  $0.42 \text{ mWh cm}^{-2}$ . A maximum energy density of  $1.87 \text{ mWh cm}^{-2}$  is achieved at a low power density of  $0.41 \text{ mW cm}^{-2}$ . In addition, the strengthened Si-Ge sp- $\mu$ ED shows stable cycling stability at a high power density of  $1.28 \text{ mW cm}^{-2}$ , further demonstrating the good energy storage performance. As the mechanical properties of the strengthened Si-Ge sp- $\mu$ ED have been improved, the cycling stability is significantly improved (Figure 4d). A capacity retention of  $67\%$  could be achieved for 50 charge/discharge cycles. Meanwhile, the coulombic efficiency could be kept above  $85\%$ . The inevitable volume change still leads to the compromise of the coulombic efficiency, which need further improvement by controlling the microstructure in the microelectrode.<sup>[54]</sup> Figure 4e

shows the SEM image of the strengthened Si-Ge sp- $\mu$ ED after cycling. The smooth surface of the Si-Ge sp- $\mu$ ED (inset in Figure 4e) wrinkled after cycling.<sup>[46,55–57]</sup> In contrast to the fractured Si-Ge sp- $\mu$ ED (Figure 3b), the wrinkles indicate that the PAAm effectively mitigates the strain induced by the volumetric variation during the charge/discharge cycles.<sup>[40]</sup> As a result, the cycling stability of the strengthened Si-Ge sp- $\mu$ ED has been significantly improved.

Based on the high-performance of the strengthened Si-Ge sp- $\mu$ EDs, we further used them to assemble a full lithium-ion microbattery. The commercial  $\text{LiMn}_2\text{O}_4$  was used as the cathode material and coated on the Al foil. The charge/discharge profiles and cycling performance of the  $\text{LiMn}_2\text{O}_4$  were first measured to confirm the actual capacity of the as-prepared cathode (Figure S12, Supporting Information). Subsequently, the amount of the  $\text{LiMn}_2\text{O}_4$  was matched to the capacity of the strengthened Si-Ge sp- $\mu$ EDs ( $14 \text{ } \mu\text{Ah}$ ). The assembled microbattery is shown in Figure 5a. The strengthened Si-Ge sp- $\mu$ ED and  $\text{LiMn}_2\text{O}_4$  coated Al foil was sealed in a capillary tube to prevent the permeation of the air and water. Figure 5a shows a small volume of the cylinder battery prototype as compared to other electric components. Keeping in mind that the diameter of the glass tube is still much larger than the diameter of the Si-Ge sp- $\mu$ ED, the footprint area can easily be further reduced.

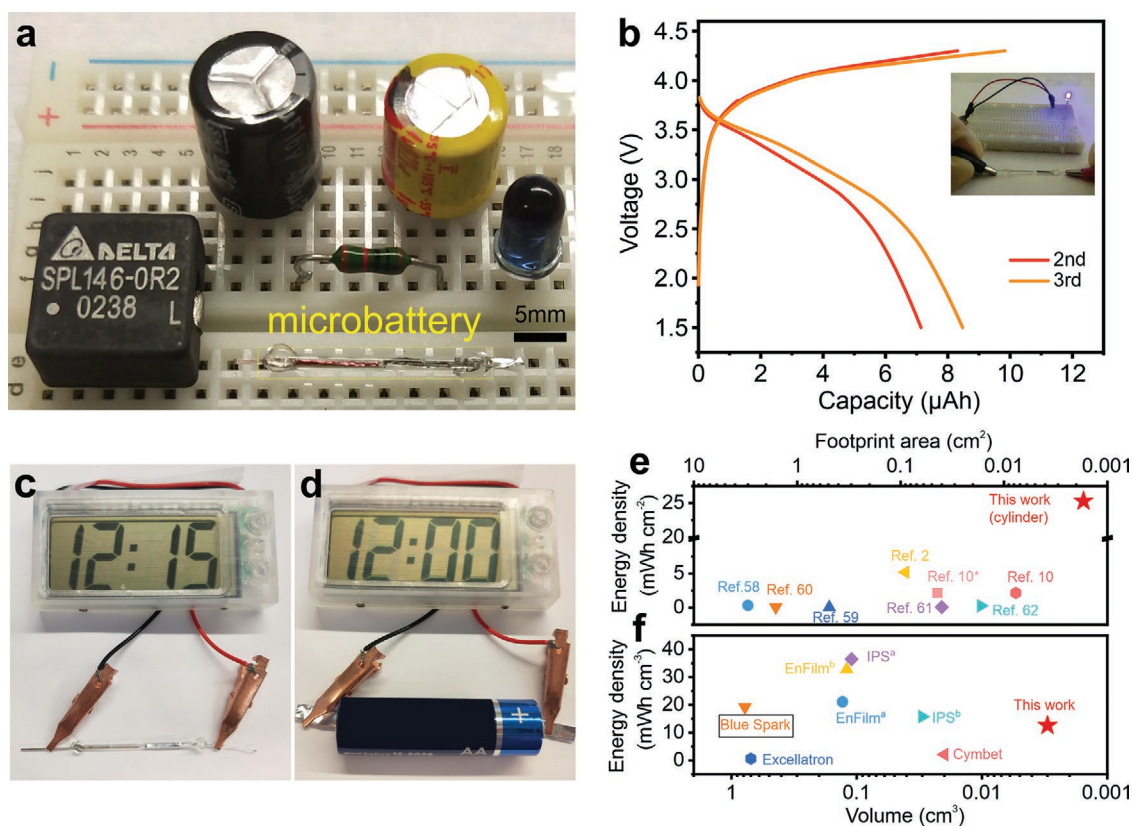


**Figure 5.** a) Photograph of cylinder full microbattery and other common electric components. b) Charge/discharge profiles of cylinder full microbattery at  $0.83 \text{ mA cm}^{-2}$ , the inset shows the digital photograph of the switched-on LED. Photographs of a digital watch powered by c) cylinder full microbattery and d) commercial AA battery. e) Comparison of the areal energy density of cylinder microbattery with reported microbatteries (\* denotes the value based on the inner footprint area). f) The comparison of volumetric energy density of cylinder microbattery with commercial microbatteries (the square symbol denotes the primary battery).

Figure 5b shows the charge/discharge profiles of the tubular microbattery, which delivers a maximum capacity of  $14 \mu\text{Ah}$  and energy of  $41 \mu\text{Wh}$  in a single battery package (Figure S13, Supporting Information). Normalized by the footprint area and volume, the areal and volumetric capacity reach  $5 \text{ mAh cm}^{-2}$  and  $3 \text{ mAh cm}^{-3}$  (Figure S14, Supporting Information). The inset in Figure 5b demonstrates that the as-fabricated cylinder microbattery can successfully light a LED bulb with a power consumption of  $60 \text{ mW}$ . Toward the low power consumption application, the tubular microbattery can continuously power a digital watch for at least  $15 \text{ min}$  (Figure 5c), indicating it could be a possible alternative for the conventional AA battery with a very large footprint area (Figure 5d).

More specifically, Figure 5e compares the areal energy density of the reported microbatteries (taking the smallest footprint area into account).<sup>[2,10,58–62]</sup> Apparently, these microbatteries show inferior areal energy density. Microbatteries with large footprint area feature thin-film design. Therefore, the areal energy density is limited by the low mass loading of the active materials. When the footprint areas decrease to  $10 \text{ mm}^2$ , even technologies based on porous and interconnected scaffolds-based, fail to guarantee high areal capacity. Intriguingly, the spiral microelectrode is based on the thin-film system. However, the transformation from a thin film to a 3D configuration not only retains the benefits of the thin-film but also increases

the mass loading within a limited footprint area. As a result, a cylinder-capacitor-like placed microbattery (vertical placement) based on the Si–Ge sp- $\mu\text{ED}$  delivers a record-high energy density of  $25.3 \text{ mWh cm}^{-2}$ . At this energy level, pairing the cathode materials at the microscale is still simple and straightforward. However, taking advantage of recently developed nanomembrane assembly approaches such as magnetic origami and field-assisted self-assembly, the area capacity could be pushed even further because the footprint area increases only a little when the rolling path is increased.<sup>[63]</sup> With further improved microanodes, the design of the microcathodes will become important as it may be a limiting factor for the overall performance of microbatteries. Figure 5f further compares the volume energy density of the as-developed cylinder microbattery with other commercial microbatteries.<sup>[13]</sup> The device volume of  $100 \text{ mm}^3$  is regarded as the margin of current microbattery technologies. Below  $100 \text{ mm}^3$ , the energy density drops dramatically. However, our prototype microbattery based on the strengthened Si–Ge sp- $\mu\text{ED}$  exhibits an energy density of  $12.6 \text{ mWh cm}^{-3}$  at an ultrasmall volume of  $3 \text{ mm}^3$  (including the tube package), showing the promising future in advancing current microbattery technologies.

In conclusion, the spiral microelectrode accomplishes a high mass loading and a short charge transfer pathway at a minimal footprint area, which enhances the areal capacity of the

microelectrode. Furthermore, the PAAm strengthening layer in the spiral microelectrode effectively resolves the challenge of the cracks induced by the significant volume variations during the charge/discharge cycles and thereby leads to a stable cycling performance. As a result, the strengthened Si–Ge sp- $\mu$ ED delivers a maximum areal capacity of 1053  $\mu\text{Ah cm}^{-2}$  and 67% capacity retention over 50 cycles. Moreover, a cylinder microbattery was constructed by using the strengthened Si–Ge sp- $\mu$ ED as the anode. Enabled by the high performance of the strengthened Si–Ge sp- $\mu$ ED, the cylinder microbattery delivers a record high areal energy density of 25.3  $\text{mWh cm}^{-2}$  at an ultrasmall footprint of 0.17  $\text{mm}^2$  and a volumetric energy density of 12.6  $\text{mWh cm}^{-3}$  at a small volume of 3  $\text{mm}^3$ , which surpasses the performance of most of the current microbattery technologies. Therefore, the newly developed sp- $\mu$ EDs set a new direction toward high-performance microbatteries that could be used for miniaturized electronic devices.

## Experimental Section

**Fabrication of Si–Ge sp- $\mu$ EDs:** The stress-actuation process was used for the fabrication of Si–Ge sp- $\mu$ EDs. First, AZ-5214E photoresist (Microchemicals GmbH, Germany) was spin-coated at 4500 rpm for 45 s. A sequential exposure with inverse and positive mode was applied to the photoresist to define the size of nanomembrane and rolling-direction. Subsequently, Au (20 nm), Si (60 nm), and Ge (20 nm) were vacuum-deposited onto the patterned chip by electron beam evaporation (Plassys and BOC Edwards FL400, Germany) at a deposition rate of 1, 1.5, and 3  $\text{\AA s}^{-1}$ , respectively. The thickness of different layers were measured and confirmed by the stylus profilometer (DektakXT, Bruker). For the thin-film electrode with different thickness increase factors, the thickness of Si and Ge was multiplied by certain thickness increase factors. The obtained nanomembranes were self-rolled-up in dimethyl sulfoxide (DMSO). The prepared Si–Ge sp- $\mu$ EDs were collected and dried with a critical point drier (CPD) (Autosamdri-931, Tousimis Research Corp.) The Si–Ge sp- $\mu$ EDs were strengthened through the soaking of 0.5 wt.% PAAm aqueous solution.

**Materials Characterization:** The morphologies of the samples were acquired by an SEM (Zeiss DSM982, Gemini, Germany) operated at 5 kV. XRD was performed by a Philips X'Pert PRO MPD diffractometer (Co  $K\alpha$  radiation,  $\lambda = 1.5418 \text{ \AA}$ ). Raman spectra were collected using a Raman microscope with a laser wavelength of 442 nm (LabRAM HR Evolution, HORIBA Scientific). The residual stress of each individual layer was analyzed by wafer curvature measurements. A DektakXT (Bruker) stylus profilometer was used to measure the curvature of a 2-in. silicon wafer before and after deposition of each layer. Stress distribution was calculated using the stress toolbox integrated in the device software.

**Electrochemical Characterizations:** The fabrication of the full cell is schematically illustrated in Figure S15, Supporting Information. Briefly, the Si–Ge sp- $\mu$ EDs were taped onto a nickel strip by silver paste. The counter electrodes were prepared by melting lithium onto titanium wires. Two electrodes were inserted into the capillary tube with a diameter of 0.95 mm. For the full cell, the capillary tube with a diameter of 0.5 mm was used. To prevent short-circuit in the course of operation, two electrodes with a minimum distance of 1 mm were placed. 1 M  $\text{LiPF}_6$  was dissolved in a mixture of ethylene carbonate (EC), diethyl carbonate (DEC), and dimethyl carbonate (DMC) (1:1:1 by weight, BASF). 2.0 v% vinylene carbonate (VC, Aldrich) was added to the above solution and used as the electrolyte. Then, the electrolyte was infused into the capillary tube and sealed by the photocurable epoxy. All cells were assembled in an argon-filled glove box (MBraun, Germany). For comparison, Si–Ge compound nanomembranes deposited on copper current collector were assembled in CR2032 coin cells, in which lithium foil was used as the counter electrode and glass fibers were used as the

separator. For the full microbattery, the cathode materials, consisting of commercial  $\text{LiMn}_2\text{O}_4$  powders, super-P, and polyvinylidene fluoride (PVDF) with a weight ratio of 6:3:1, were coated onto the aluminum strips, which were further assembled with Si–Ge sp- $\mu$ EDs in the capillary tube.

Galvanostatic charge/discharge measurements were carried out in the voltage range of 0.01–2.5 V versus  $\text{Li/Li}^+$  by using an Arbin BT2000 system. Cyclic voltammetry (CV) tests were carried out between 0.01 to 2.5 V at a scan rate of 0.1  $\text{mV s}^{-1}$  by an electrochemical workstation (MULTIAUTOLAB/M101, Metrohm Autolab). Impedance tests were carried out from 100 000 to 0.01 Hz with an amplitude of 10 mV. The lithium electrode was directly used as the counter and reference electrode for the measurement.

**Finite Element Simulation:** To simulate experimental structures, Ansys Academic 17.2 was used. The simulation used was Static structural module. Mechanical parameters for silicon were: 140 GPa (Young's modulus), 0.265 (Poisson's ratio), 165 MPa (tensile yield strength), 3.2 GPa (compressive yield strength), and 165 MPa (tensile ultimate strength). Mechanical parameters for germanium were: 103 GPa (Young's modulus), 0.275 (Poisson's ratio), 135 MPa (tensile yield strength), 2 GPa (compressive yield strength), and 135 MPa (tensile ultimate strength). To implement built-in strain, thermal expansion coefficient (TEC) of the material was used. For the simplification of simulations, TEC for Ge was considered as  $-1 \text{ }^\circ\text{C}^{-1}$ , and  $0 \text{ }^\circ\text{C}^{-1}$  for Si. The strain used in the simulation was 0.00014 (Au), 0.00072 (Ge), and 0.00151 (Si). One side of the trilayer was fixed, and sides along rolling direction were fixed by frictionless support. For the mesh, curvature size function was used with the fine span angle and maximum face size as 4  $\mu\text{m}$ . Thermal strain was applied gradually over 1 s with the minimum and maximum time step intervals as 10  $\mu\text{s}$  and 10 ms, respectively. Analysis settings were based on large deflection and full Newton–Raphson option.

## Supporting Information

Supporting Information is available from the Wiley Online Library or from the author.

## Acknowledgements

H.T., L.L., and Y.L. acknowledge financial support from the China Scholarship Council (CSC). O.G.S. acknowledges financial support by the Leibniz Program of the German Research Foundation (SCHM 1298/26-1). The authors thank Dr. Baunack Stefan for the support on SEM operation. The authors appreciate Xiaoqun Zhao for the roll-up process section, as well as Ronny Engelhard, Barbara Eichler, Sandra Nestler, Carol Schmidt, Martin Bauer, and Lisa Shröder for the support in the clean room facilities. The authors also thank Ulrike Nitzsche for the technical assistance with the calculating cluster.

## Conflict of Interest

The authors declare no conflict of interest.

## Keywords

high energy density, lithium-ion microbatteries, spiral microelectrodes, stress-actuation

Received: April 15, 2020

Revised: June 14, 2020

Published online: July 23, 2020

- [1] P. Zhang, F. Wang, M. Yu, X. Zhuang, X. Feng, *Chem. Soc. Rev.* **2018**, 47, 7426.
- [2] J. I. Hur, L. C. Smith, B. Dunn, *Joule* **2018**, 2, 1187.
- [3] Z. S. Wu, Y. Z. Tan, S. Zheng, S. Wang, K. Parvez, J. Qin, X. Shi, C. Sun, X. Bao, X. Feng, K. Müllen, *J. Am. Chem. Soc.* **2017**, 139, 4506.
- [4] X. Shi, S. Pei, F. Zhou, W. Ren, H. M. Cheng, Z. S. Wu, X. Bao, *Energy Environ. Sci.* **2019**, 12, 1534.
- [5] Z. Lei, L. Liu, H. Zhao, F. Liang, S. Chang, L. Li, Y. Zhang, Z. Lin, J. Kröger, Y. Lei, *Nat. Commun.* **2020**, 11, 299.
- [6] H. Tan, Z. Liu, D. Chao, P. Hao, D. Jia, Y. Sang, H. Liu, H. J. Fan, *Adv. Energy Mater.* **2018**, 8, 1800685.
- [7] K. Shen, J. Ding, S. Yang, *Adv. Energy Mater.* **2018**, 8, 1800408.
- [8] Y. Wang, B. Liu, Q. Li, S. Cartmell, S. Ferrara, Z. D. Deng, J. Xiao, *J. Power Sources* **2015**, 286, 330.
- [9] Lithium-ion cells: VARTA Microbattery, <https://www.varta-microbattery.com/en/products/lithium-ion-cells> (accessed: March **2020**).
- [10] K. Sun, T. S. Wei, B. Y. Ahn, J. Y. Seo, S. J. Dillon, J. A. Lewis, *Adv. Mater.* **2013**, 25, 4539.
- [11] J. F. M. Oudenhoven, L. Baggetto, P. H. L. Notten, *Adv. Energy Mater.* **2011**, 1, 10.
- [12] C. Liu, E. I. Gillette, X. Chen, A. J. Pearse, A. C. Kozen, M. A. Schroeder, K. E. Gregorczyk, S. B. Lee, G. W. Rubloff, *Nat. Nanotechnol.* **2014**, 9, 1031.
- [13] S. Ferrari, M. Loveridge, S. D. Beattie, M. Jahn, R. J. Dashwood, R. Bhagat, *J. Power Sources* **2015**, 286, 25.
- [14] T. S. Arthur, D. J. Bates, N. Cirigliano, D. C. Johnson, P. Malati, J. M. Mosby, E. Perre, M. T. Rawls, A. L. Prieto, B. Dunn, *MRS Bull.* **2011**, 36, 523.
- [15] J. W. Long, B. Dunn, D. R. Rolison, H. S. White, *Chem. Rev.* **2004**, 104, 4463.
- [16] A. A. Talin, D. Ruzmetov, A. Kolmakov, K. McKelvey, N. Ware, F. El Gabaly, B. Dunn, H. S. White, *ACS Appl. Mater. Interfaces* **2016**, 8, 32385.
- [17] A. Pearse, T. Schmitt, E. Sahadeo, D. M. Stewart, A. Kozen, K. Gerasopoulos, A. A. Talin, S. B. Lee, G. W. Rubloff, K. E. Gregorczyk, *ACS Nano* **2018**, 12, 4286.
- [18] J. H. Pikul, J. Liu, P. V. Braun, W. P. King, *J. Power Sources* **2016**, 315, 308.
- [19] Y. Jin, B. Zhu, Z. Lu, N. Liu, J. Zhu, *Adv. Energy Mater.* **2017**, 7, 1700715.
- [20] Y. Zhong, X. Xia, F. Shi, J. Zhan, J. Tu, H. J. Fan, *Adv. Sci.* **2016**, 3, 1500286.
- [21] B. Wang, W. Li, T. Wu, J. Guo, Z. Wen, *Energy Storage Mater.* **2018**, 15, 139.
- [22] A. Magasinski, P. Dixon, B. Hertzberg, A. Kvit, J. Ayala, G. Yushin, *Nat. Mater.* **2010**, 9, 353.
- [23] Q. Zhang, H. Chen, L. Luo, B. Zhao, H. Luo, X. Han, J. Wang, C. Wang, Y. Yang, T. Zhu, M. Liu, *Energy Environ. Sci.* **2018**, 11, 669.
- [24] T. Song, H. Cheng, H. Choi, J. H. Lee, H. Han, D. H. Lee, D. S. Yoo, M. S. Kwon, J. M. Choi, S. G. Doo, H. Chang, J. Xiao, Y. Huang, W. I. Park, Y. C. Chung, H. Kim, J. A. Rogers, U. Paik, *ACS Nano* **2012**, 6, 303.
- [25] X. Zhao, C. M. Hayner, M. C. Kung, H. H. Kung, *Adv. Energy Mater.* **2011**, 1, 1079.
- [26] J. R. Szczech, S. Jin, *Energy Environ. Sci.* **2011**, 4, 56.
- [27] W. Ren, C. Wang, L. Lu, D. Li, C. Cheng, J. Liu, *J. Mater. Chem. A* **2013**, 1, 13433.
- [28] Y. Yang, S. Liu, X. Bian, J. Feng, Y. An, C. Yuan, *ACS Nano* **2018**, 12, 2900.
- [29] P. R. Abel, A. M. Chockla, Y. M. Lin, V. C. Holmberg, J. T. Harris, B. A. Korgel, A. Heller, C. B. Mullins, *ACS Nano* **2013**, 7, 2249.
- [30] T. Song, H. Cheng, K. Town, H. Park, R. W. Black, S. Lee, W. I. Park, Y. Huang, J. A. Rogers, L. F. Nazar, U. Paik, *Adv. Funct. Mater.* **2014**, 24, 1458.
- [31] X. Wang, Y. Chen, O. G. Schmidt, C. Yan, *Chem. Soc. Rev.* **2016**, 45, 1308.
- [32] J. Deng, X. Lu, L. Liu, L. Zhang, O. G. Schmidt, *Adv. Energy Mater.* **2016**, 6, 1600797.
- [33] K. G. Gallagher, S. E. Trask, C. Bauer, T. Woehrle, S. F. Lux, M. Tschuch, P. Lamp, B. J. Polzin, S. Ha, B. Long, Q. Wu, W. Lu, D. W. Dees, A. N. Jansen, *J. Electrochem. Soc.* **2016**, 163, A138.
- [34] M. Ko, S. Chae, J. Cho, *ChemElectroChem* **2015**, 2, 1645.
- [35] J. K. Lee, C. Oh, N. Kim, J. Y. Hwang, Y. K. Sun, *J. Mater. Chem. A* **2016**, 4, 5366.
- [36] L. Hu, H. Wu, S. S. Hong, L. Cui, J. R. McDonough, S. Bohy, Y. Cui, *Chem. Commun.* **2011**, 47, 367.
- [37] O. G. Schmidt, K. Eberl, *Nature* **2001**, 410, 168.
- [38] Y. Mei, A. A. Solovev, S. Sanchez, O. G. Schmidt, *Chem. Soc. Rev.* **2011**, 40, 2109.
- [39] D. Karnaushenko, T. Kang, O. G. Schmidt, *Adv. Mater. Technol.* **2019**, 4, 1800692.
- [40] L. Liu, M. Zhu, S. Huang, X. Lu, L. Zhang, Y. Li, S. Wang, L. Liu, Q. Weng, O. G. Schmidt, *J. Mater. Chem. A* **2019**, 7, 14097.
- [41] L. Zhang, J. Deng, L. Liu, W. Si, S. Oswald, L. Xi, M. Kundu, G. Ma, T. Gemming, S. Baunack, F. Ding, C. Yan, O. G. Schmidt, *Adv. Mater.* **2014**, 26, 4527.
- [42] C. Yan, W. Xi, W. Si, J. Deng, O. G. Schmidt, *Adv. Mater.* **2013**, 25, 539.
- [43] S. Huang, L. Zhang, X. Lu, L. Liu, L. Liu, X. Sun, Y. Yin, S. Oswald, Z. Zou, F. Ding, O. G. Schmidt, *ACS Nano* **2017**, 11, 821.
- [44] D. Karnaushenko, T. Kang, V. K. Bandari, F. Zhu, O. G. Schmidt, *Adv. Mater.* **2020**, 32, 1902994.
- [45] J. Jiang, Y. Li, J. Liu, X. Huang, *Nanoscale* **2011**, 3, 45.
- [46] W. Si, I. Mönch, C. Yan, J. Deng, S. Li, G. Lin, L. Han, Y. Mei, O. G. Schmidt, *Adv. Mater.* **2014**, 26, 7973.
- [47] X. H. Liu, L. Zhong, S. Huang, S. X. Mao, T. Zhu, J. Y. Huang, *ACS Nano* **2012**, 6, 1522.
- [48] D. Bermejo, M. Cardona, *J. Non-Cryst. Solids* **1979**, 32, 405.
- [49] Z. Wang, F. Mo, L. Ma, Q. Yang, G. Liang, Z. Liu, H. Li, N. Li, H. Zhang, C. Zhi, *ACS Appl. Mater. Interfaces* **2018**, 10, 44527.
- [50] J. Evans, C. A. Vincent, P. G. Bruce, *Polymer* **1987**, 28, 2324.
- [51] W. Liu, S. W. Lee, D. Lin, F. Shi, S. Wang, A. D. Sendek, Y. Cui, *Nat. Energy* **2017**, 2, 17035.
- [52] Y. Liu, Y. Zhu, Y. Cui, *Nat. Energy* **2019**, 4, 540.
- [53] K. Stokes, G. Flynn, H. Geaney, G. Bree, K. M. Ryan, *Nano Lett.* **2018**, 18, 5569.
- [54] M. Sternad, M. Forster, M. Wilkening, *Sci. Rep.* **2016**, 6, 31712.
- [55] A. Al-Obeidi, D. Kramer, C. V. Thompson, R. Mönig, *J. Power Sources* **2015**, 297, 472.
- [56] C. Yu, X. Li, T. Ma, J. Rong, R. Zhang, J. Shaffer, Y. An, Q. Liu, B. Wei, H. Jiang, *Adv. Energy Mater.* **2012**, 2, 68.
- [57] J. Y. Chung, T. Q. Chastek, M. J. Fasolka, H. W. Ro, C. M. Stafford, *ACS Nano* **2009**, 3, 844.
- [58] S. W. Song, K. C. Lee, H. Y. Park, *J. Power Sources* **2016**, 328, 311.
- [59] H. S. Lee, S. Kim, K. B. Kim, J. W. Choi, *Nano Energy* **2018**, 53, 225.
- [60] S. Zheng, Z. S. Wu, F. Zhou, X. Wang, J. Ma, C. Liu, Y. B. He, X. Bao, *Nano Energy* **2018**, 51, 613.
- [61] H. Ning, J. H. Pikul, R. Zhang, X. Li, S. Xu, J. Wang, J. A. Rogers, W. P. King, P. V. Braun, *Proc. Natl. Acad. Sci. USA* **2015**, 112, 6573.
- [62] J. H. Pikul, H. G. Zhang, J. Cho, P. V. Braun, W. P. King, *Nat. Commun.* **2013**, 4, 1732.
- [63] F. Gabler, D. D. Karnaushenko, D. Karnaushenko, O. G. Schmidt, *Nat. Commun.* **2019**, 10, 3013.